ECS TECHNICAL REPORT 2013/07
http://www.dur.ac.uk/resources/ecs/research/technical_reports/2013_07.pdf

# Local maximum entropy shape functions based FE-EFGM coupling

Z. Ullah, C. E. Augarde and W. M. Coombs,*

**Abstract:** In this paper, a new method for coupling the finite element method (FEM) and the element-free Galerkin method (EFGM) is proposed for linear elastic and geometrically nonlinear problems using local maximum entropy shape functions in the EFG zone of the problem domain. These shape functions possess a weak Kronecker delta property at the boundaries which provides a natural way to couple the EFG and the FE regions as compared to the use of moving least square basis functions. In this new approach, there is no need for interface/transition elements between the EFG and the FE regions or any other special treatment for shape function continuity across the FE-EFG interface. One- and two-dimensional linear elastic and two-dimensional geometrically nonlinear benchmark numerical examples are solved by the new approach to demonstrate the implementation and performance of the current approach.

## 1. Introduction

The element-free Galerkin method (EFGM) [1] is superior to the finite element method (FEM) in terms of accuracy and convergence but is computationally more expensive. Therefore, it is more practical to use the EFGM only in regions of a problem domain requiring its high accuracy where it can outperform the FEM, while using the FEM in the remaining part of the problem domain. For this combined method, proper coupling between the FEM and the EFGM is essential for accurate results.

Previous research has used interface elements between EFG and FE regions [2, 3, 4]. This approach was motivated by the incompatibility between the MLS shape functions within the EFG region for the approximation of the field variables, and the standard polynomial shape functions in the FE region. Hybrid shape functions of these elements, consisting of both types of shape functions, have previously been formed using blending functions [2]. In [5], to facilitate the direct imposition of essential boundary conditions, a strip of FEs was used on the essential boundary while the EFGM was used in the remaining part of the problem domain, and the FE and the EFG regions were coupled using the procedure proposed in [2], i.e. using interface elements. The FE-EFGM coupling procedure of [2] was also extended for the case of nodal integration used in the EFG region in [6]. A continuous blending method for the FE-EFGM coupling was introduced in [7, 8] with some advantages compared to the FE-EFGM coupling procedure of [2] since ramp functions and the use of the FE nodes as the EFG nodes is not required, therefore, EFG nodes can also be added within the transition region. Lagrange multipliers were used for linear elastic analysis with the same type of coupling in [9], and idea that was later extended

*School of Engineering and Computing Sciences, Durham University.

to nonlinear reinforced concrete problems in [10], where reinforcement was modelled with the FEM and concrete with the EFGM. In [11], a transition (or bridging region) was used for coupling between the FEM and a meshless method. The transition region was discretized by particles, which were independent of both the FE and meshless nodes. A detailed review of this type of coupling between the EFGM and the FEM can be found in [12]. A coupled FE-EFGM was also proposed in [13] for the simulation of automotive crash tests, in which areas with very high deformation were modelled with the EFGM. This work used constraints to ensure the continuity of the shape functions across the FE-EFGM interface without using interface elements. A slight variation of the FE-EFGM coupling with interface elements [2], in which there was no need for a pre-existing transition region between the FE and EFG regions was proposed in [14]. The method was applied to the simulation of linear elastic fracture mechanics problems, including mode-I, mode-II and mixed mode problems. The area near the crack was modelled with the EFGM, while the FEM was used in the remaining part of the problem domain, just as suggested above. A coupled FE-EFGM procedure based on a collocation approach was proposed in [15], in which at the interface between the FE and the EFG regions, fictitious nodal values were converted to real nodal displacements using the MLS shape functions and were assigned back to the FE nodes. as a final example in [16], the FE-EFGM coupling procedure of [2] was used to couple the EFGM with the FEM to conveniently impose the essential boundary conditions in the dynamic soil structure interaction problems.

Maximum entropy (max-ent) concepts provide an alternative way to calculate the shape functions for meshless methods and are based on the concept of informational entropy [17, 18, 19, 20]. These shape functions were first introduced in [21] for the construction of polygonal interpolants. In [17] informational entropy was referred to as a lack of knowledge or uncertainty. [19, 20] introduced the principle of max-ent as being the maximization of the informational entropy, resulting in a least biased (or feasible solution) for the probability distribution in the case of insufficient data. This idea was used in [21] to solve the under-determined system of equations appearing in the case of the polygonal interpolants for the case ($n > 3$) with constant and linear reproducing constraints, where $n$ is the number of sides of the polygon. Shape functions derived for the polygonal interpolation in [21] are not ideal for meshless methods as they are defined over the global problem domain. The non-local and non-interpolating characteristics of these shape functions are highlighted in [22], where the (more useful) local max-ent formulations were introduced and incorporated into meshless modelling of linear and nonlinear elasticity. The weak Kronecker delta property of these shape functions was observed, and its correspondence with the MLS approach was also highlighted. Compact support shape functions were derived using Gaussian weight functions (or priors) in [22], work which was extended in [23] to any weight function (or generalized prior). First-order consistent max-ent shape functions [23] were then extended to second order in [24] and higher order in [25] and max-ent was used in [26] for the automatic calculation of the nodal domain of influence within a meshless method. Other recent examples of the use of max-ent in meshless methods can be found in [27, 28, 29, 30, 31].

The outline of this paper is as follows. The modified EFGM with max-ent shape functions is described in §2. A detailed description of the proposed FE-EFGM coupling procedure based on max-ent shape functions in two-dimensions is given in §3, followed by explanations of the FE and max-ent shape functions in 3.1. One- and two- linear elastic numerical examples are then given in §4 to show the implementation and performance of the coupling procedure for linear elastic problems. The proposed coupled FE-EFGM approach is then extended to geometrically nonlinear problems in §5, followed by two numerical examples in §6. Concluding remarks are

given in §7.

## 2. The element-free Galerkin method

Consider a two-dimensional problem (for clarity, where extension to three-dimensional is trivial) defined in the domain $\Omega$ and bounded by $\Gamma$. The equilibrium equation at a point $\mathbf{x}$ is written as

$$\boldsymbol{\nabla}^T \boldsymbol{\sigma} + \mathbf{b}_f = 0 \qquad \text{in } \Omega, \tag{1}$$

where $\boldsymbol{\sigma} = \begin{bmatrix} \sigma_{xx} & \sigma_{yy} & \tau_{xy} \end{bmatrix}^T$ is the Cauchy stress vector, $\mathbf{b}_f = \begin{bmatrix} b_{f_x} & b_{f_y} \end{bmatrix}^T$ is the body force vector, where $b_{f_x}$ and $b_{f_y}$ are the body forces in $x$ and $y$ directions respectively and $\boldsymbol{\nabla}$ is the differential operator, and is given by $\boldsymbol{\nabla} = \begin{Bmatrix} \frac{\partial}{\partial x} & 0 \\ 0 & \frac{\partial}{\partial y} \\ \frac{\partial}{\partial y} & \frac{\partial}{\partial x} \end{Bmatrix}$.

The boundary conditions associated with Equation (1) are

$$\mathbf{u} = \bar{\mathbf{u}} \qquad \text{on } \Gamma_u, \tag{2a}$$

$$\boldsymbol{\sigma}\mathbf{n} = \bar{\boldsymbol{t}} \qquad \text{on } \Gamma_t, \tag{2b}$$

where Equation (2a) is essential or Dirichlet boundary condition and Equation (2b) is natural or Neumann boundary condition. Here $\mathbf{u} = \begin{bmatrix} u_x & u_y \end{bmatrix}^T$ is the displacement vector, where $u_x$ and $u_y$ are the displacements in $x$ and $y$ directions, and $\mathbf{n} = \begin{bmatrix} n_x & n_y \end{bmatrix}^T$ are the outward unit normal to the boundary $\Gamma$, $\bar{\boldsymbol{t}}$ is the prescribed traction on the traction boundary $\Gamma_t$ and $\bar{\mathbf{u}}$ is the prescribed displacement on the essential boundaries $\Gamma_u$. In the conventional EFGM, MLS shape functions are used for the approximation of the field variables, which do not satisfy the Kronecker delta property and Lagrange multipliers are used to impose the essential boundary conditions, therefore the constrained Galerkin weak form are used, the details of which can be found in [1, 32]. By using max-ent shape functions for the approximation of the field variables, instead of the conventional MLS shape function, the Galerkin weak form equation is written as

$$\int_{\Omega} \delta \left(\boldsymbol{\nabla}\mathbf{u}\right)^T \mathbf{D} \left(\boldsymbol{\nabla}\mathbf{u}\right) d\Omega + \int_{\Omega} \delta\mathbf{u}^T \mathbf{b}_f d\Omega + \int_{\Gamma_t} \delta\mathbf{u}^T \bar{\mathbf{t}} d\Gamma = 0, \tag{3}$$

where $\mathbf{D}$ is the matrix of material constants. Due to the weak Kronecker delta property of the max-ent shape functions, there is no need to use the Lagrange multipliers for the imposition of essential boundary conditions. The essential boundary conditions are implemented directly as in the case of the FEM. After discretizing the problem with a set of nodes, displacement at a point of interest $\mathbf{x}$ is written as

$$\mathbf{u}^h(\mathbf{x}) = \begin{Bmatrix} u_x \\ u_y \end{Bmatrix} = \sum_{i=1}^{n} \begin{bmatrix} \phi_i & 0 \\ 0 & \phi_i \end{bmatrix} \begin{Bmatrix} u_{xi} \\ u_{yi} \end{Bmatrix} = \sum_{i=1}^{n} \boldsymbol{\phi}_i \mathbf{u}_i, \tag{4}$$

where $\mathbf{u}^h(\mathbf{x})$ is an approximation of the displacements at a point $\mathbf{x}$, $n$ is the number of nodes in the support of point $\mathbf{x}$, $\boldsymbol{\phi}_i$ is a matrix of the max-ent shape functions for node $i$ at a point $\mathbf{x}$ and $\mathbf{u}_i$ are known as fictitious nodal values or nodal parameters. Using Equations (4) in (3) and after simplification, the final discrete system of linear equation is written as

$$\mathbf{K}\mathbf{u} = \mathbf{f}, \tag{5}$$

where

$$\mathbf{K}_{ij} = \int_{\Omega} \mathbf{B}_i^T \mathbf{D} \mathbf{B}_j d\Omega, \tag{6}$$

$$\mathbf{f}_i = \int_{\Gamma_t} \phi_i \bar{\mathbf{t}} d\Gamma + \int_{\Omega} \phi_i \mathbf{b}_f d\Omega, \tag{7}$$

$$\mathbf{B}_i = \begin{bmatrix} \frac{\partial \phi_i}{\partial x} & 0 \\ 0 & \frac{\partial \phi_i}{\partial y} \\ \frac{\partial \phi_i}{\partial y} & \frac{\partial \phi_i}{\partial x} \end{bmatrix}, \tag{8}$$

$$\mathbf{D} = \frac{\overline{E}}{1-\overline{\nu}^2} \begin{bmatrix} 1 & \overline{\nu} & 0 \\ \overline{\nu} & 1 & 0 \\ 0 & 0 & \frac{1-\overline{\nu}}{2} \end{bmatrix}, \tag{9}$$

$$\overline{E} = \begin{cases} E & \text{for plane stress,} \\ \frac{E}{1-\nu^2} & \text{for plane strain,} \end{cases} \tag{10a}$$

$$\overline{\nu} = \begin{cases} \nu & \text{for plane stress,} \\ \frac{\nu}{1-\nu} & \text{for plane strain,} \end{cases} \tag{10b}$$

where $\nu$ is the Poisson's ratio and $E$ is the modulus of elasticity. To perform the integrations in Equations (6) and (7) numerically, the problem domain $\Omega$ and traction boundary $\Gamma_t$ are divided into a number of non-overlapping background cells as shown in Figure 1.

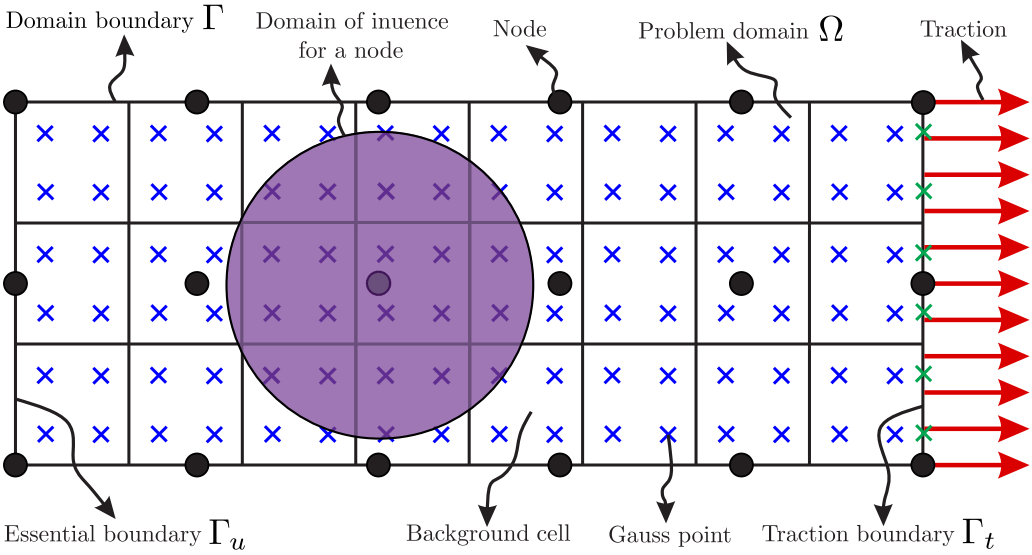


Figure 1: The EFGM problem discretization

## 3. FE-EFGM Coupling using max-ent shape functions

In the FE-EFGM coupling based on the interface elements [2], MLS shape functions are used in the EFG zone for the approximation of the field variables. The MLS shape functions do not possess the Kronecker delta property like the FE shape functions and due to this reason interface elements are introduced between the FE and the EFG zones [2, 3, 4], to properly couple the two regions. The shape functions for the interface elements are hybrid shape functions of the FE and the EFG shape functions to make the displacement continuous across the FE-EFGM interface. The details of the FE-EFGM coupling based on the interface elements is not given here and can be found in the relevant literature. In this paper, max-ent shape functions are used in the EFG region of the problem domain, which provide a natural way to couple the FEM

and the EFGM without using interface elements or transition regions between the FE and EFG zones because of their weak Kronecker delta property at the boundaries. A sample mixed FE and EFG discretization is shown in Figure 2, where $\Omega_E$ and $\Omega_F$ are the EFG and the FE regions and $\Gamma$ is the boundary between these two regions. The nodes on the boundary $\Gamma$ between the EFG and FE regions, shown in green in Figure 2, are used in the displacement approximation for both the EFG and the FE regions. Shape functions for the two regions, i.e. FE and EFG are explained in the

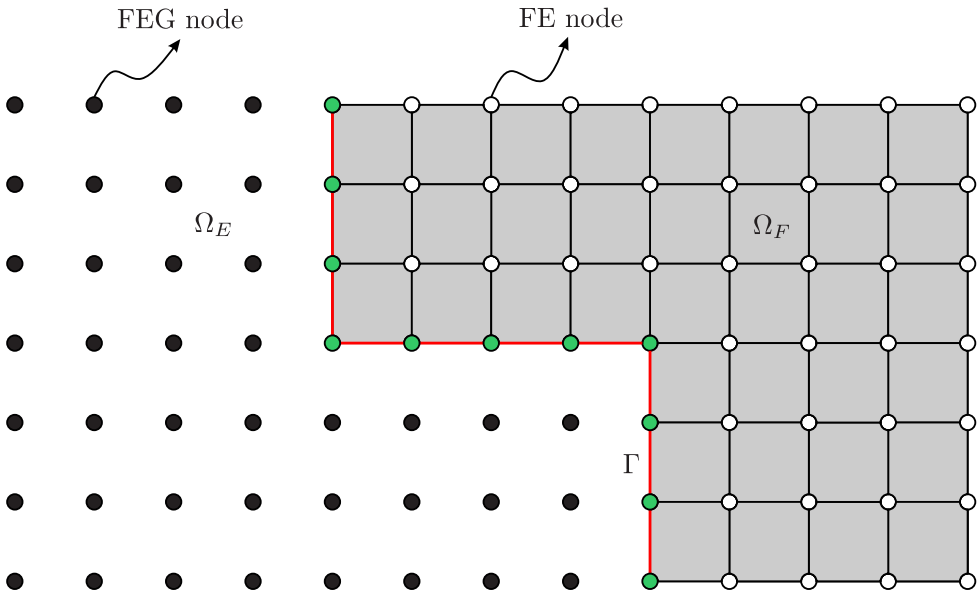


Figure 2: FE-EFGM coupling using max-ent shape functions

next section.

**3.1. Shape functions.** Displacement can be approximated at point **x** in a similar way in the two regions, i.e.

$$u^h(\mathbf{x}) = \sum_{i=1}^{n} \widetilde{N}_i(\mathbf{x})\, u_i, \tag{11}$$

where $u^h(\mathbf{x})$ is the approximate displacement component at point **x**, $\widetilde{N}_i(\mathbf{x})$ is either the FE, the EFG or interface element shape function for node $i$ evaluated at point **x**, $n$ is the number of nodes in support of point **x** and $u_i$ are either nodal displacements in the case of the FEM, or nodal parameters in case of the EFGM.

**3.1.1. Finite element.** In the FE region four node iso-parametric quadrilateral elements are used in two-dimensional problems, for which shape functions are the standard bilinear shape functions [33], i.e.

$$N_i = \frac{1}{4}(1+\xi_i\xi)(1+\eta_i\eta), \tag{12}$$

where $\xi$ and $\eta$ are natural or parent coordinates, $i$ is the node numbering, while $\xi_i$ and $\eta_i$ are the nodal coordinates of the parent element.

**3.1.2. Maximum entropy shape functions.** In this case, the max-ent shape functions are used in the EFG regions of the of the problem domain. The max-ent concept comes from information theory [18] where a measure of the amount of

information or uncertainty of a finite scheme is termed information entropy and is given as

$$H(p_1, ...., p_n) = -\sum_{i=1}^{N} p_i \log p_i, \tag{13}$$

where $p_1, ...., p_n$ are $n$ probabilities of $n$ mutually independent events. The most likely probability distribution is obtained by using Jaynes' principle of max-ent [20], i.e. maximising Equation (13) subject to constraints $\sum_{i=1}^{n} p_i = 1$ and $\sum_{i=1}^{n} p_i g_r(x_i) = \langle g_r(x) \rangle$ , where $\langle g_r(x) \rangle$ is the expectation of a function $g_r(x)$. The max-ent approach can be used to derive shape functions by seeing an analogy between the probabilities above and the shape function values themselves. A useful local shape function formulation can be obtained (see [23] for details) by incorporating prior distributions, $w_i$, which can be regarded as weight functions that provide compact support, and then maximising the following

$$H(\phi, w) = -\sum_{i=1}^{n} \phi_i \log\left(\frac{\phi_i}{w_i}\right), \tag{14}$$

again subject to the standard constant and linearly reproducing constraints

$$\sum_{i=1}^{n} \phi_i = 1, \qquad \sum_{i=1}^{n} \phi_i x_i = x \text{ and } \sum_{i=1}^{n} \phi_i y_i = y. \tag{15}$$

The max-ent shape functions follow as

$$\phi_i = \frac{Z_i}{Z} \tag{16}$$

where

$$Z_i = w_i e^{-\lambda_1 \widetilde{x}_i - \lambda_2 \widetilde{y}_i} \text{ and } Z = \sum_{j=1}^{n} Z_j, \tag{17}$$

in which $w_i$ is the weight function associated with node $i$, evaluated at point $\mathbf{x} = (x, y)^T$ , $\widetilde{x_i} = x_i - x$ and $\widetilde{y_i} = y_i - y$ are shifted coordinates. $n$ is the number of nodes in support at $\mathbf{x}$ and $\lambda_1$ and $\lambda_2$ are Lagrange multipliers which can be found from

$$(\lambda_1, \lambda_2) = \text{argmin} F(\lambda_1, \lambda_2), \qquad \text{where } F(\lambda_1, \lambda_2) = \log(Z). \tag{18}$$

$F$ is a convex function and here Newton's method is used to solve Equation (18) to find these Lagrange multipliers. Shape function derivatives are obtained as [34]

$$\nabla \phi_i = \phi_i \left( \nabla f_i - \sum_{i=1}^{n} \phi_i \nabla f_i \right), \tag{19}$$

where

$$\nabla f_i = \frac{\nabla w_i}{w_i} + \boldsymbol{\lambda} + \widetilde{\mathbf{x}}_i \left[ H^{-1} - H^{-1} A \right] \text{ and } A = \sum_{k=1}^{n} \phi_k \widetilde{\mathbf{x}}_k \otimes \frac{\nabla w_k}{w_k}. \tag{20}$$

Where H is the Hessian matrix and the dyadic product $\otimes$ of two vector $\mathbf{a}$ and $\mathbf{b}$ is a second order tensor, i.e. $\mathbf{a} \otimes \mathbf{b}$ defined as $\mathbf{a} \otimes \mathbf{b} = \mathbf{a}\mathbf{b}^T$. Cubic spline weight functions are used in this paper, which is given as follows for one-dimensional case

$$w = \begin{cases} \frac{2}{3} - 4r^2 + 4r^3 & \text{for } r \leq \frac{1}{2}, \\ \frac{4}{3} - 4r + 4r^2 - \frac{4}{3} r^3 & \text{for } \frac{1}{2} < r \leq 1, \\ 0 & \text{for } r > 1, \end{cases} \tag{21}$$

where $r = \frac{d_i}{d_{mi}}$ is the normalized radius, where $d_i = \|x - x_i\|$ is the distance between the node $i$ and point of interest $x$ and $d_{mi}$ is the domain of influence of node $i$. The size of domain of influence for a node $i$ is $d_{mi} = d_{max} c_i$, where $d_{max}$ is a scaling parameter, for static analysis its value ranges from 2.0 to 4.0 [35] and $c_i$ is the distance between two adjacent nodes in uniformly distributed nodes. For two-dimensional problems, a rectangular nodal domain of influence is used in this paper, for which a tensor product of one-dimensional form [35, 32] is used.

## 4. Numerical examples

One- and two-dimensional linear elastic numerical examples are now presented to demonstrate the implementation and performance of the proposed coupled FE-EFGM formulation. The results from the proposed approach are also compared with the conventional FE-EFGM coupling with the interface elements [2] and other possible alternatives.

**4.1. One-dimensional bar.** Consider a one-dimensional bar of unit length subjected to body force and fixed at a point $x = 0$. The geometry, coordinate system, loading and boundary conditions are shown in Figure 3. The analytical solutions for

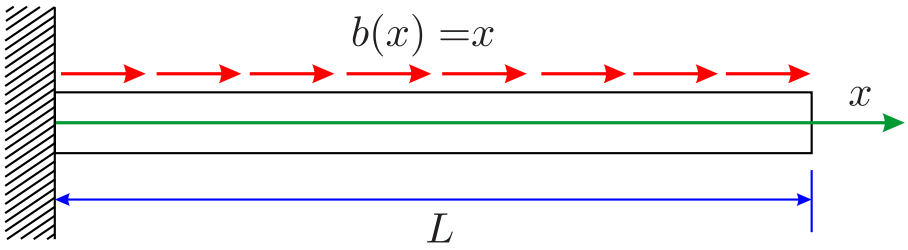


Figure 3: Geometry and loading for 1D bar problem

the displacement and stress field for this problem are given as

$$u(x) = \frac{1}{E}\left(\frac{1}{2}x - \frac{x^3}{6}\right) \text{ and } \sigma(x) = \left(\frac{1-x^2}{2}\right), \tag{22}$$

where $E = 1.0$ is used. The problem was solved using the conventional FE-EFGM coupling, i.e. using MLS shape functions within the EFG region and using a transition or interface region between the EFG and the FE regions (MLS with interface). The problem discretizations with four FE, an interface element and five EFG background cells is shown in Figure 4(a). The same problem is also solved with the proposed FE-EFGM coupling, i.e. using max-ent shape functions within the EFG region and without the interface element between the FE and the EFG regions (max-ent without interface). The problem discretization for the proposed coupling with four FE and six EFG background cells is shown in Figure 4(b). For comparison the same problem is also solved with the same discretization as shown in Figure 4(b) but using MLS shape functions within the EFG regions (MLS without interface). In all three cases, the essential boundary conditions are implemented directly because of the use of the FE region on the essential boundary side.

Initially, the problem was solved with $d_{max} = 2.5$ in the EFG region. The comparison between the nodal displacements along the length of the bar in all the three cases and the analytical solution is shown in Figure 5(a). The nodal displacements coincide and there is no apparent difference. The same problem is further analysed with the same three types of discretization but this time using $d_{max} = 3.5$. In this case the comparison between the nodal displacements along the length of the bar in

all three cases, and the analytical solution are shown in Figure 5(b). This time the results for the nodal displacements of the two cases, i.e. MLS with interface and max-ent without interface are in good agreement with the analytical solution. The deviation of the nodal displacements from the analytical solution for the MLS without interface can be clearly seen in Figure 5(b). This shows the importance of the interface element, when using MLS in the EFG region of the problem.

The dependence of the results on $d_{max}$ is further analysed using plots of the shape functions and shape function derivatives for all three cases. Plots for the shape functions and shape function derivatives for the MLS with interface elements with $d_{max} = 2.5$ are shown in Figures 6(a) and 6(c) respectively, and for $d_{max} = 3.5$ are shown in Figures 6(b) and 6(d) respectively. It is clear from these plots that increasing $d_{max}$ increases the number of nodes influencing the zone between the EFG and FE regions. In this case, the interface element creates a smooth blending between the EFG and the FE regions, i.e. there is no discontinuity in the shape functions and shape functions derivative on $\Gamma_E$ and $\Gamma_F$. A jump can be observed in the shape functions and shape function derivatives on $\Gamma_E$, which is the point where the shape functions change from the MLS shape functions to the interface element shape functions. For the max-ent without interface, plots for the shape functions and shape function derivatives for $d_{max} = 2.5$ are shown in Figures 7(a) and 7(c) respectively, and for $d_{max} = 3.5$ in Figures 7(b) and 7(d) respectively. In this case due to the weak Kronecker delta property of the max-ent shape functions, all the shape functions and shape function derivatives naturally blend together very smoothly on the boundary node between the EFG and the FE region. The boundary node is used for the shape functions' calculations on both the EFG and the FE region and the shape functions of all the internal nodes on the EFG side goes to zero at this node. For the MLS without interface, plots for the shape function and derivatives for $d_{max} = 2.5$ are shown in Figures 8(a) and 8(c) respectively, and for $d_{max} = 3.5$ in Figures 8(b) and 8(d) respectively. A discontinuity in the shape functions and shape function derivatives on the boundary nodes can be seen for $d_{max} = 2.5$, which is not sufficient to produce a significant deviation in the nodal displacements from the analytical solution as shown in Figure 5(a). A very clear discontinuity in the shape functions and shape function derivatives can be seen on the boundary node between the EFG and the FE region for $d_{max} = 3.5$, which produces a clear deviation in the nodal displacements from the analytical solutions as shown in Figure 5(b). This clearly shows the need for interface elements between the FE and the EFG region, when using the MLS shape functions.

For convergence studies the $L_2$ norm of error in energy $\|e\|$, suggested in [36] are used, that is

$$\|e\| = \left( \int_{\Omega} \mathbf{e}_{\varepsilon}^T \mathbf{D} \mathbf{e}_{\varepsilon} d\Omega \right)^{\frac{1}{2}} = \left( \int_{\Omega} \mathbf{e}_{\sigma}^T \mathbf{D}^{-1} \mathbf{e}_{\sigma} d\Omega \right)^{\frac{1}{2}}. \tag{23}$$

where $\mathbf{e}_{\varepsilon}$ and $\mathbf{e}_{\sigma}$ are errors in strains and stresses at a point $\mathbf{x}$ and are written as

$$\mathbf{e}_{\varepsilon} = \boldsymbol{\varepsilon}_{exact} - \boldsymbol{\varepsilon}_{num}, \qquad \mathbf{e}_{\sigma} = \boldsymbol{\sigma}_{exact} - \boldsymbol{\sigma}_{num}, \tag{24}$$

where $\boldsymbol{\varepsilon}_{exact}$ and $\boldsymbol{\sigma}_{exact}$ are the exact strains and stresses at a point $\mathbf{x}$, while $\boldsymbol{\varepsilon}_{num}$ and $\boldsymbol{\sigma}_{num}$ are numerical strains and stresses at the same point respectively. For this purpose, for the max-ent without interface and the MLS without interface cases, half of the problem is discretized with the FE region, and the other half is discretized with the EFG region. For the MLS with interface case, half of the problem is discretized with the FE region, and the other half is discretized with the combine interface and

the EFG regions. The number of nodes used for analysis in the problem domain in the consecutive discretizations are 11, 13, 15, 17, 19 and 21. $d_{max} = 2.5$ is used in this case. The convergence plots are shown in Figure 9, in which curves for the MLS with interface and max-ent without interface coincide with each other with almost the same rate of convergence. The MLS without interface performs poorly with high error and low rate of convergence as compared to the other two cases. For comparison, curves are also given in the same figure for the cases when the same problem is solved only with the FEM and only with the EFGM with the MLS and the max-ent shape functions. It is clear from Figure 9 that the coupled FE-EFGM performs somewhere between the pure FEM and the pure EFGM. The error in energy norm and rate of convergence for the coupled FE-EFGM also lies between the pure FEM and the pure EFGM cases. For the MLS without interface case, although at the start, the error in energy norm lies between the pure FEM and the pure EFGM cases, the rate of convergence is lower than the pure FEM case.

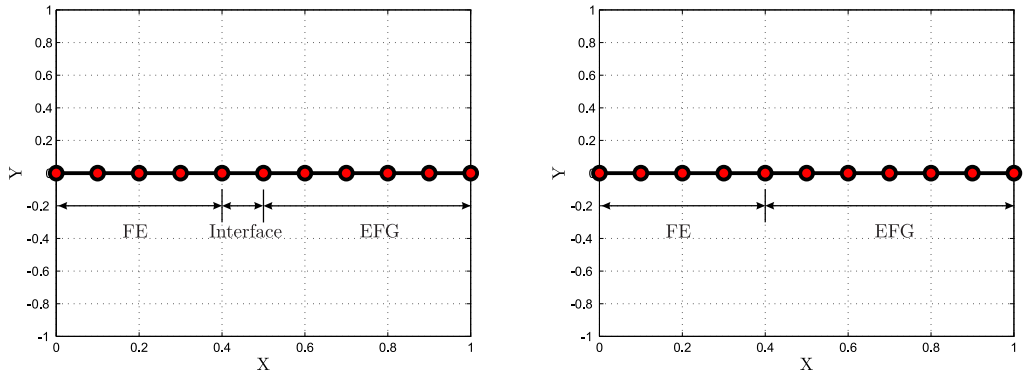


(a) with interface element (b) without interface element

Figure 4: Discretizations for the one-dimensional bar problem

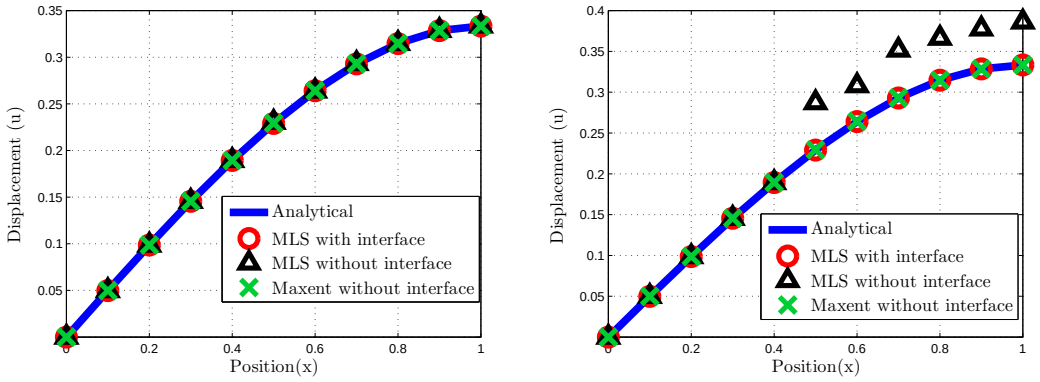


(a) $d_{max} = 2.5$ (b) $d_{max} = 3.5$

Figure 5: Displacements for the one-dimensional bar problem

**4.2. Two-dimensional cantilever beam.** The behaviour of the 2D cantilever beam subjected to parabolic traction at the free end [37] is now examined. The geometry, coordinate system, loading and boundary conditions for the problem, which are more complicated than is often appreciated [38], are given in Figure 10. The analytical solution for the displacement field is given as [39]

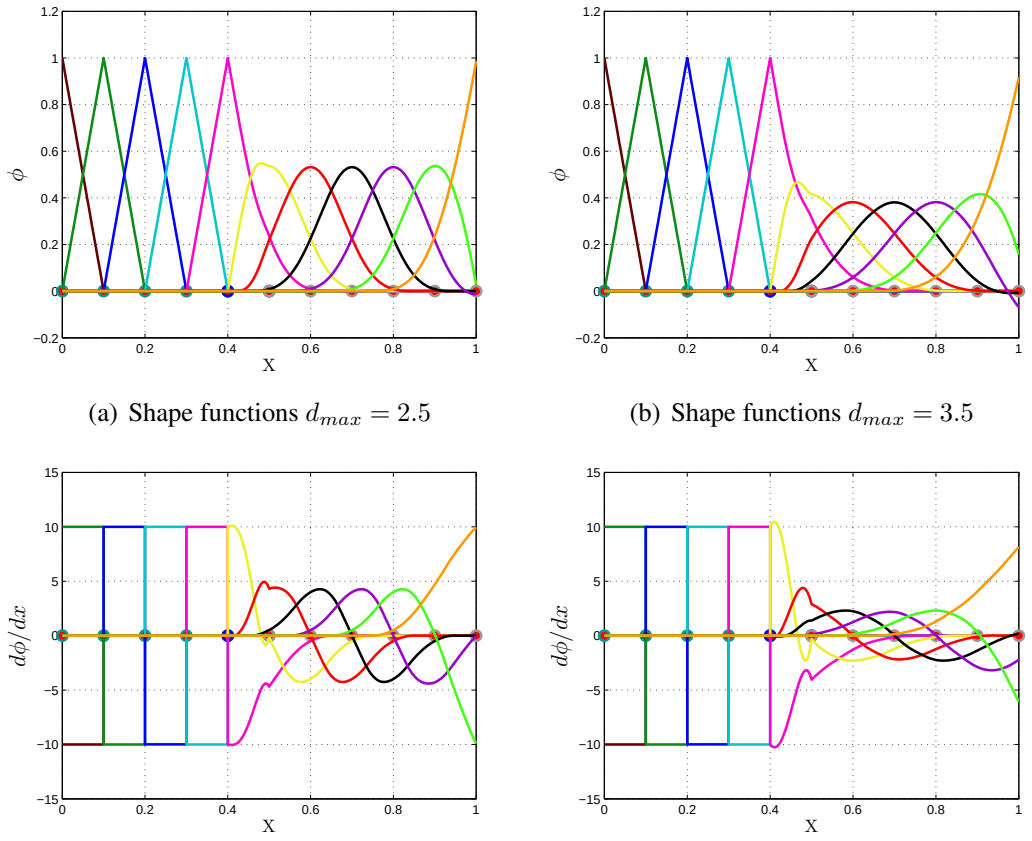


(a) Shape functions $d_{max} = 2.5$

(b) Shape functions $d_{max} = 3.5$

(c) Shape function derivatives $d_{max} = 2.5$

(d) Shape function derivatives $d_{max} = 3.5$

Figure 6: Shape functions and shape function derivatives for the one-dimensional bar problem coupling using MLS with interface elements

$$u(x,y) = \frac{Py}{6EI}\left[(6L-3x)\,x + (2+\nu)\,y^2 - \frac{3D^2}{2}(1+\nu)\right], \tag{25a}$$

$$v(x,y) = -\frac{P}{6EI}\left[3\nu y^2(L-x) + (3L-x)\,x^2\right], \tag{25b}$$

while the analytical solutions for the stress fields is

$$\sigma_{xx} = \frac{P(L-x)\,y}{I}, \tag{26a}$$

$$\sigma_{yy} = 0, \tag{26b}$$

$$\sigma_{xy} = -\frac{P}{2I}\left[\frac{D^2}{4} - y^2\right], \tag{26c}$$

where $I$ is the second moment of area. The analysis assumed a plane stress condition with $P = 1000$ , $\nu = 0.3$ , $E = 30 \times 10^6$ , $D = 12$ , $L = 48$ and unit thickness, all in compatible units. The problem was solved with the three different discretizations, i.e. the MLS with interface, the max-ent without interface and the MLS without interface. The problem is discretized with 189 $(21 \times 9)$ nodes and 160 $(20 \times 8)$ background cells, as shown in Figures 11(a) and 11(b) with interface elements and without interface elements respectively. In Figure 11(a), the first five columns (starting from the left) are the FE, and the sixth one consists of interface elements, while the rest are the EFG background cells. In Figure 11(b) the first five columns are the FE while the rest are the EFG background cells. In all three cases, essential boundary conditions are implemented directly due to the use of the FE on the essential

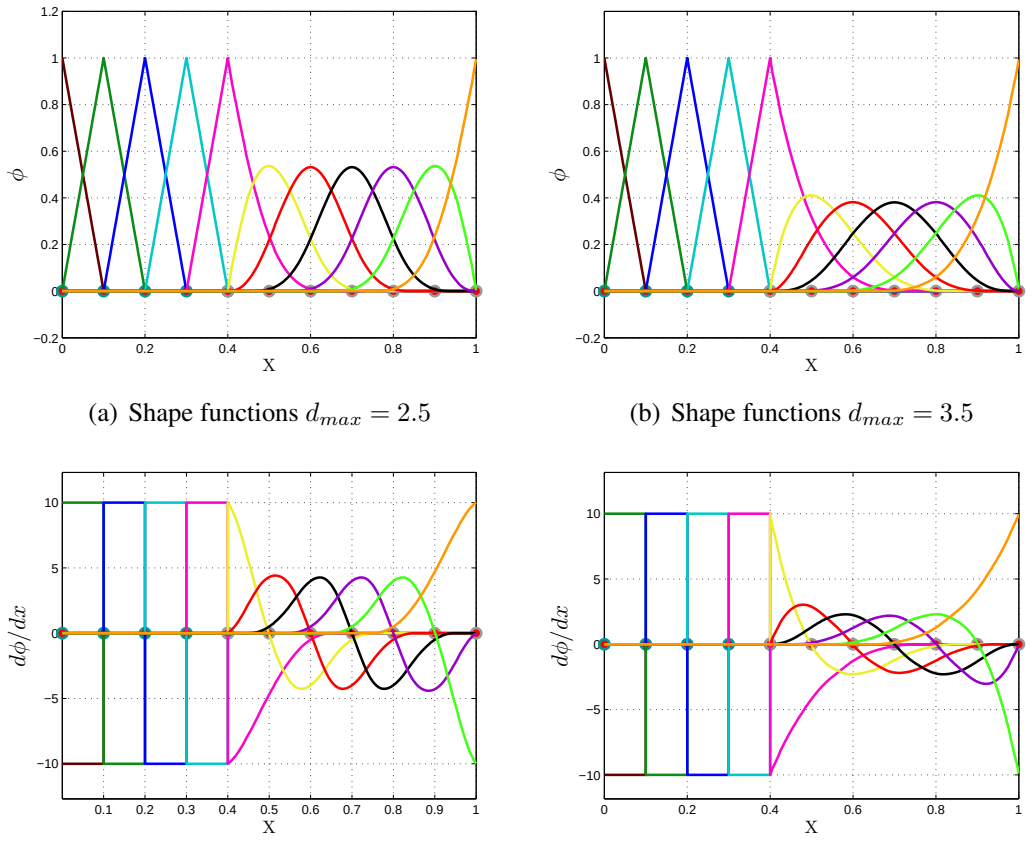


(a) Shape functions $d_{max} = 2.5$

(b) Shape functions $d_{max} = 3.5$

(c) Shape function derivatives $d_{max} = 2.5$

(d) Shape function derivatives $d_{max} = 3.5$

Figure 7: Shape functions and shape function derivatives for the one-dimensional bar problem coupling using max-ent without interface elements

boundary side.

Initially, the problem was solved with $d_{max} = 2.5$ and comparison of nodal displacement at $y = 0$, and stresses $\sigma_{xx}$ and $\sigma_{xy}$ at $x = L/2$ to the analytical solutions are shown in Figures 12(a), 12(b) and 12(c) respectively. In this case all the results are in a close agreement with the analytical solution. Next, the same problem is solved with $d_{max} = 3.5$ and the same comparison of the nodal displacement and stresses with the analytical solution are shown in Figures 13(a), 13(b) and 13(c) respectively. A very clear difference between the numerical and analytical results in the case of the MLS without interface case can be seen in these plots. The results in the case of the MLS with interface and the max-ent without interface are again in close agreement with the analytical solution. This once again verifies that there is no need for the interface elements in the coupled FE-EFGM formulation while using the max-ent shape functions within the EFG region.

To study convergence for the same problem once again the $L_2$ norm of error in energy $\|e\|$ is used. In this case 27 $(9 \times 3)$, 52 $(13 \times 4)$, and 85 $(17 \times 5)$ nodes are used in the consecutive discretizations. For the max-ent without interface and the MLS without interface cases, half of the beam is modelled with the FEM, and the other half is modelled with the EFGM. For the MLS with interface case, half of the problem is modelled with the FEM, and the other half is discretized with the combine interface elements and the EFG background cells. The convergence plots for $d_{max} = 2.5$ are shown in Figure 14(a) in which all three curves are in very close agreement with almost the same rate of convergence. The same plots

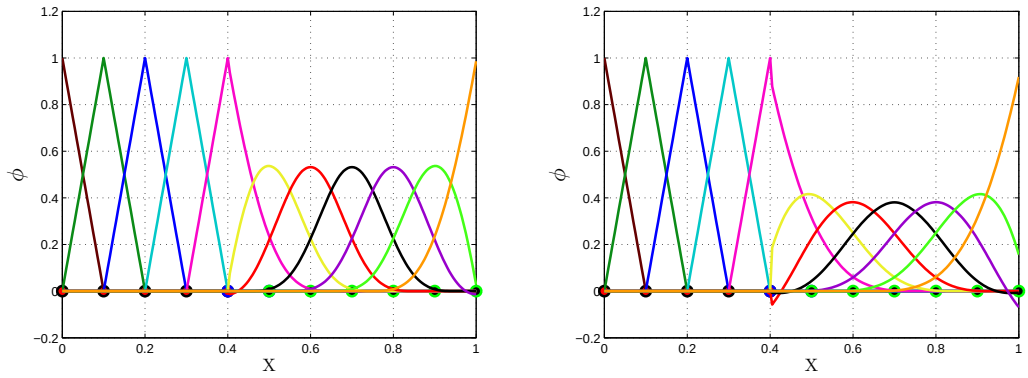


(a) Shape functions $d_{max} = 2.5$




(b) Shape functions $d_{max} = 3.5$

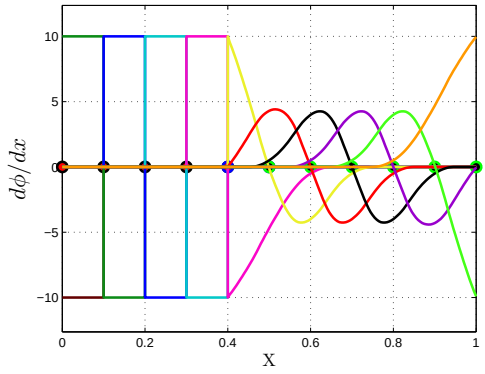


(c) Shape function derivatives $d_{max} = 2.5$

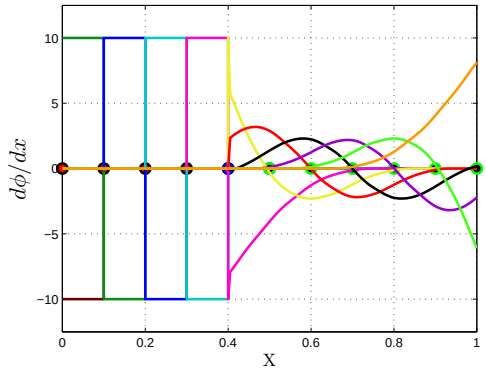


(d) Shape function derivatives $d_{max} = 3.5$

Figure 8: Shape functions and shape function derivatives for the one-dimensional bar problem coupling using MLS without interface elements

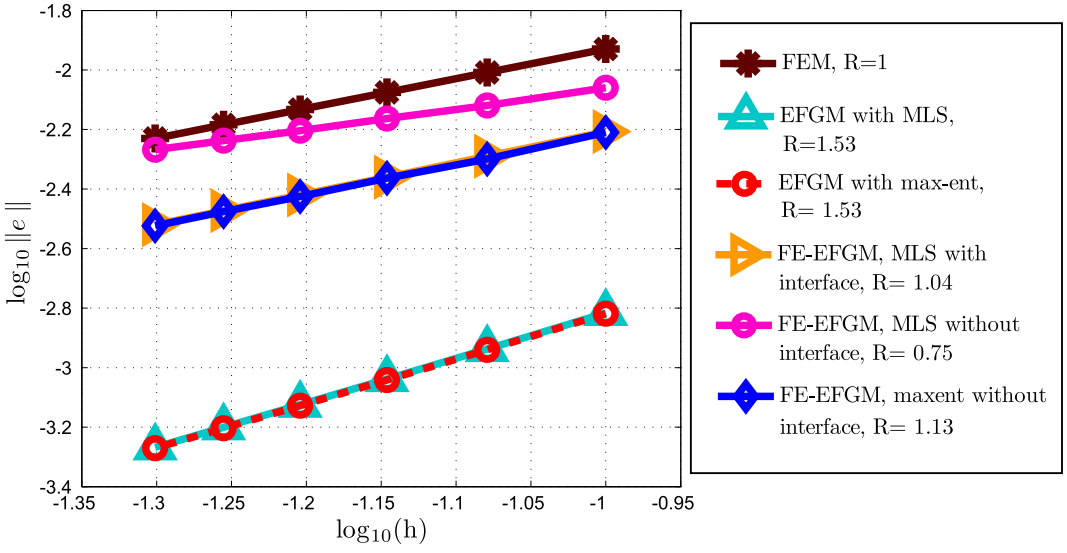


Figure 9: Convergence plots for different discretizations for the one-dimensional bar problem

for $d_{max} = 3.5$ are shown in Figure 14(b), in which the curves for the MLS with interface, and the max-ent without interface are in very close agreement with almost

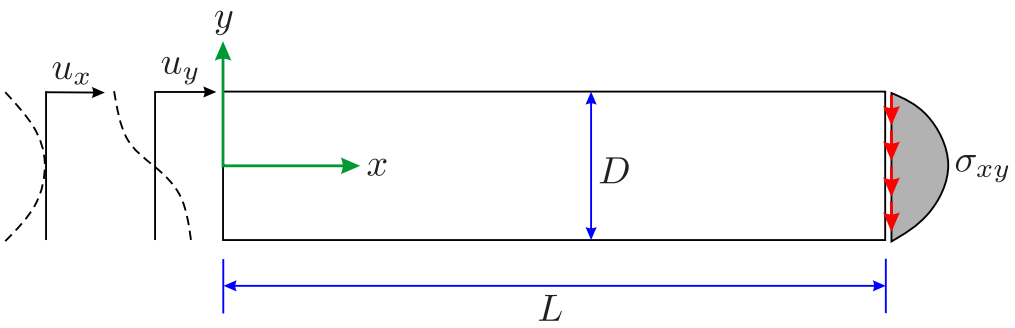


Figure 10: Geometry, boundary condition and loading for 2D beam problem

the same rate of convergence however, the error is very high in the case of MLS without interface. This once again proves the importance of the interface elements (or transition regions) in the case when using MLS shape functions within the EFG regions.

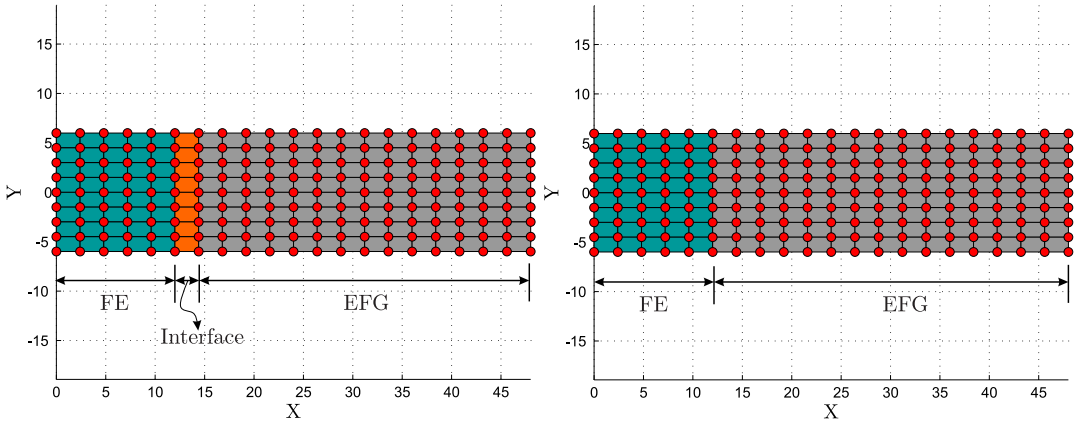


(a) with interface element (b) without interface element

Figure 11: Discretizations for the two-dimensional beam problem

**4.3. Flexible strip footing.** The third numerical example is an elastic plane strain flexible strip footing. The problem is also solved using hybrid MLPG and scaled boundary method in [40], the exact solution for which is given in [41]. The exact solution for the relative displacement between the centre of the footing and any point on the surface a horizontal distance $x$ from the centre is

$$\Delta u_y = \frac{2q\left(1-\nu^2\right)}{\pi E}\left\{(x-R)\ln|x-R| - (x+R)\ln|x+R| + 2R\ln R\right\}, \quad (27)$$

where $2R$ is the width of footing and $q$ is the uniformly distributed load (or pressure per unit length) on footing. Here, $R = 0.6$, $q = 1000$ as shown in Figure 15. Due to symmetry only one-half of the problem, shown in gray in Figure 15, was modelled with appropriate boundary conditions. The coupled FE-EFGM discretization of the problem with and without an interface region are shown in Figures 16(a) and 16(b) respectively. In Figure 16(a), the region shown in gray from $y = 7.2$ to $y = 8$ and from $x = 0$ to $x = 0.8$ is the EFG region, followed by a strip of interface elements shown in orange and the rest is the FE region. In Figure 16(b), the region shown in gray from $y = 7.2$ to $y = 8$ is the EFG region and the rest is the FE region.

Initially, the problem is solved with the MLS with interface using the discretization shown in Figure 16(a). The imposition of the essential boundary conditions on

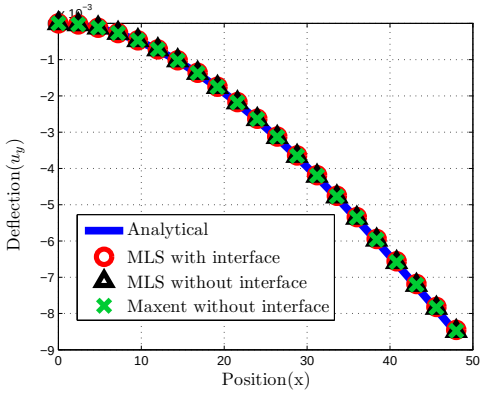


(a) $u_y$ at $y = 0$

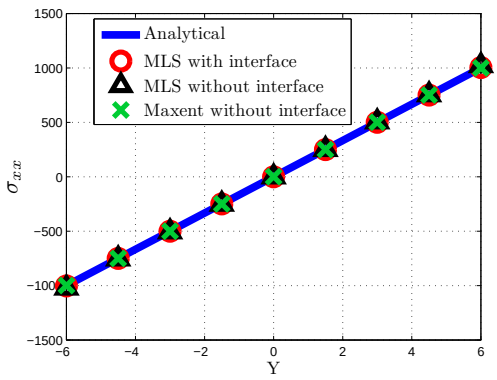


(b) $\sigma_{xx}$ at $x = L/2$

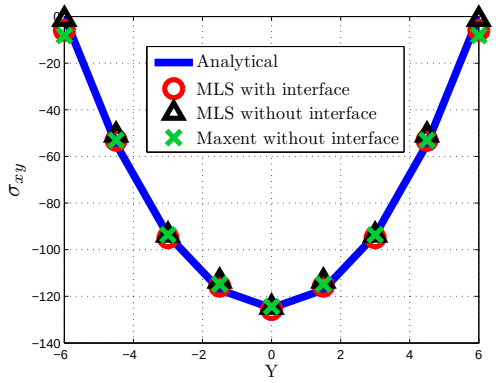


(c) $\sigma_{xy}$ at $x = L/2$

Figure 12: Displacements and stresses for the two-dimensional beam problem at $d_{max} = 2.5$

the right and bottom edge is straightforward because of the use FE on these boundaries, while on the left edge it is more involved due to the presence of both the FE and the EFG regions. On the left edge, Lagrange multipliers are used to impose the essential boundary conditions for the first six nodes from the top, while the direct method is used for the rest of the nodes. The discretization shown in Figure 16(b), is used for the MLS without interface and max-ent without interface formulations. For the MLS without interface, Lagrange multipliers are used to impose the essential boundary conditions for the first five nodes from the top on the left edge, while the direct method is used for the rest of the boundary nodes. In the case of max-ent without interface, all the essential boundary conditions are implemented directly. The problem is first solved with $d_{max} = 2.5$ for all three cases and a comparison of the surface deflection with the analytical solution is given in Figure 17(a). Here all the numerical results are in close agreement with the analytical solution. The same problem is again solved with the same parameters but changing $d_{max}$ to 3.8 and a comparison between the numerical surface deflection in all three cases and the analytical solution is given in Figure 17(b). Once again, the results from the MLS with interface and max-ent without interface are in close agreement with each other and the exact solution. However a very clear difference can be seen in the results for the MLS without interface case, especially near the centre of the footing. Contour plots for the vertical displacements $(u_y)$ at $d_{max} = 3.8$ for a region of the problem domain near the footing with dimensions $(2 \times 2)$ are also given in Figures 18(a), 18(b) and 18(c) for the MLS with interface, the MLS without interface and the max-ent with

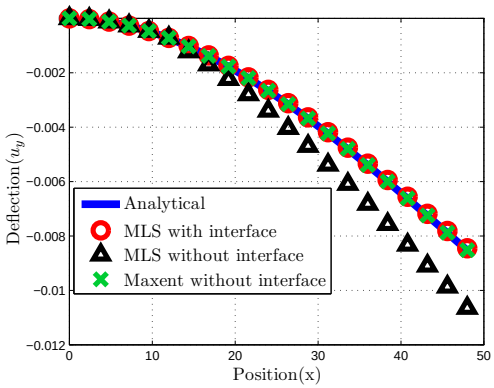


(a) $u_y$ at $y = 0$

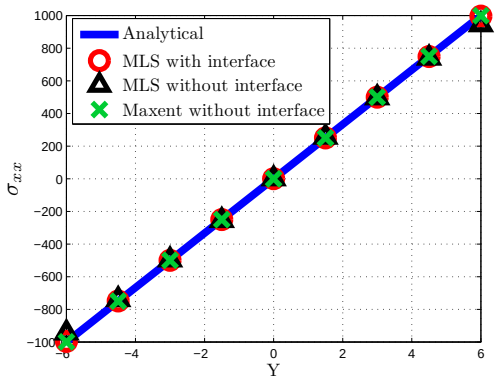


(b) $\sigma_{xx}$ at $x = L/2$

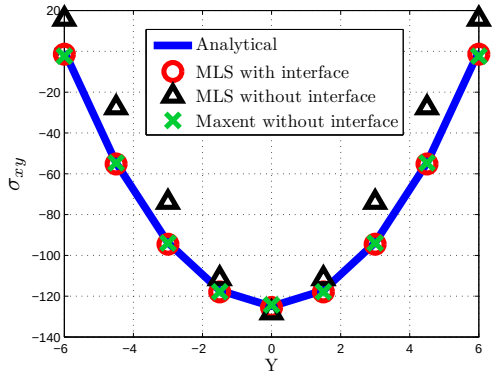


(c) $\sigma_{xy}$ at $x = L/2$

Figure 13: Displacements and stresses for the two-dimensional beam problem at $d_{max} = 3.5$

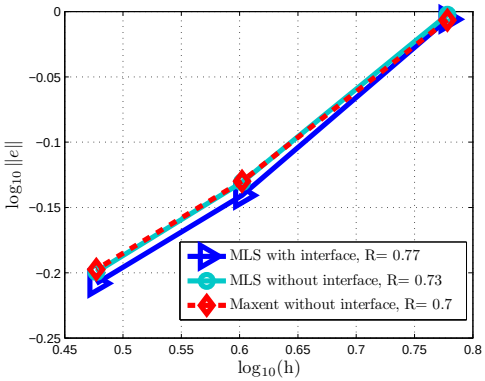


(a) $d_{max} = 2.5$

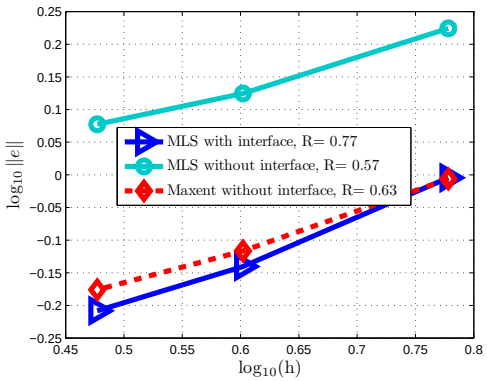


(b) $d_{max} = 3.5$

Figure 14: Convergence plots for different discretizations and at different $d_{max}$ for the two-dimensional beam problem

interface cases respectively. The $u_y$ contours are very smooth throughout the regions in the MLS with interface and the max-ent without interface cases, while the results in the case of the MLS without interface are disappointing. The curves in this case are clearly in error, especially near the centre of the footing. The results once again verify that there is no need for a transition region between the FE and the EFG regions, when using max-ent shape functions within the EFG region. The results also

verifies the fact that the transition region is unavoidable in cases when using MLS within in the EFG region.

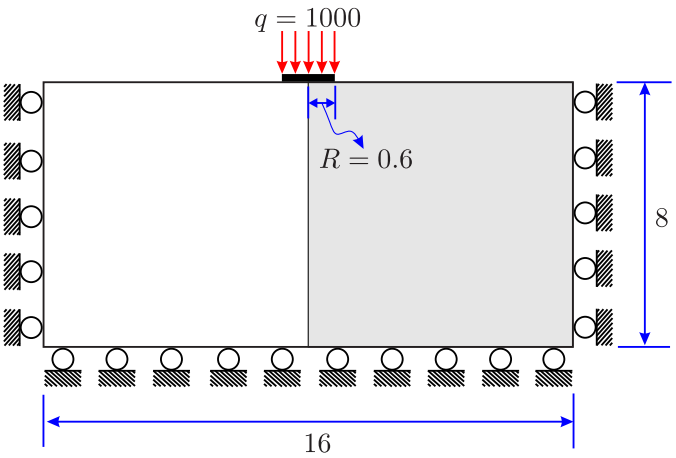


Figure 15: Geometry, boundary condition and loading for the flexible strip footing problem

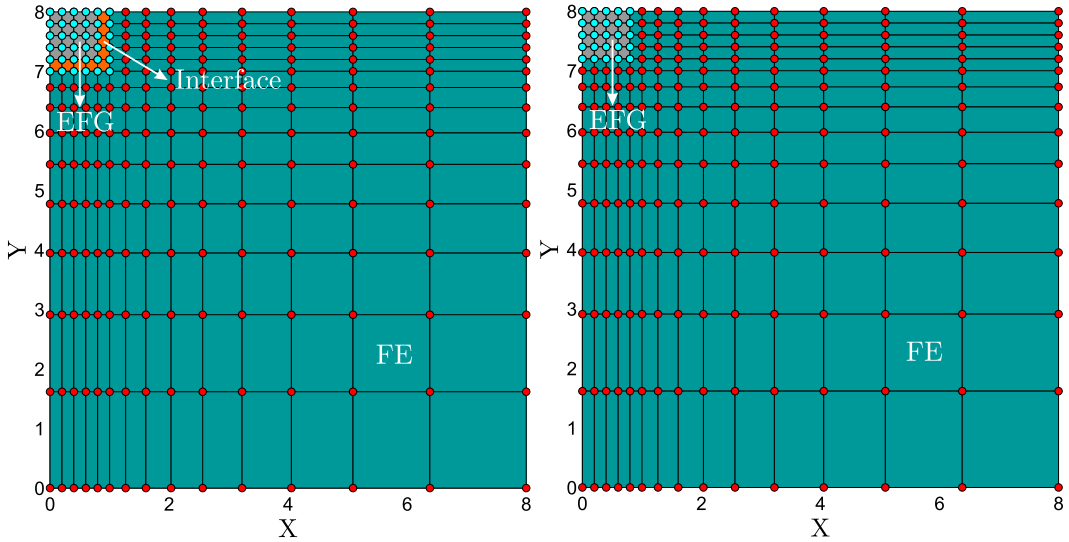


(a) with interface element (b) without interface element

Figure 16: Discretizations for the flexible strip footing problem

## 5. Extension to nonlinear problems

Having demonstrated above the accuracy of the proposed approach using coupled FE with max-ent based EFG regions, the next step is to move to nonlinear problems. In this section, the proposed coupled FE-EFGM approach is extended to geometrically nonlinear problems. Here an updated Lagrangian formulation is used to model finite deformation, in which all the kinematical variables are referred to the current configuration. The deformation gradient is used, which is the fundamental measure of deformation, to provide the relationship between the current and reference configurations, given by

$$\mathbf{F} = \frac{\partial \mathbf{x}}{\partial \mathbf{X}}, \tag{28}$$

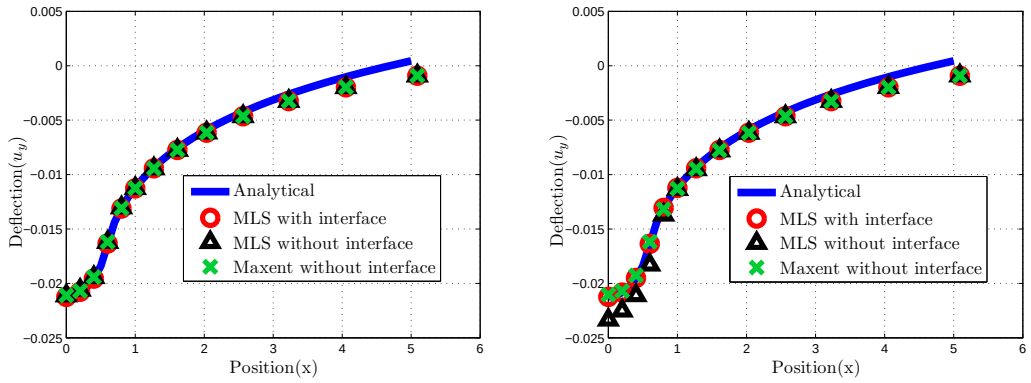


(a) $d_{max} = 2.5$ (b) $d_{max} = 3.8$

Figure 17: Surface deflection for different discretization for the flexible strip footing problem

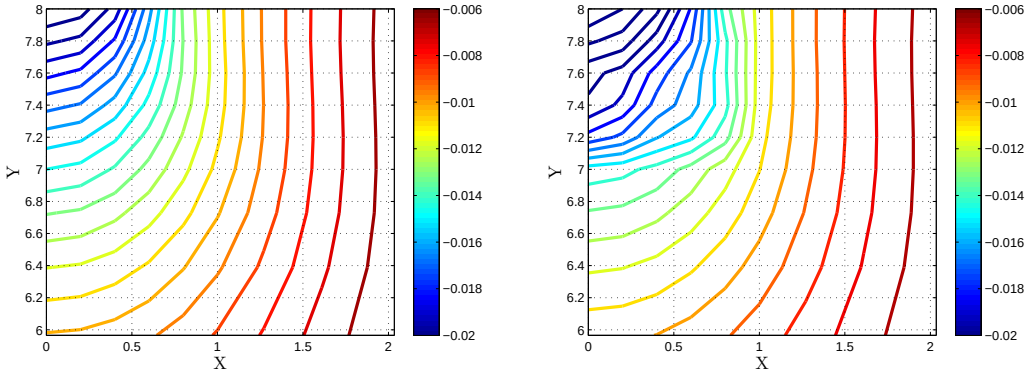


(a) MLS with interface (b) MLS without interface

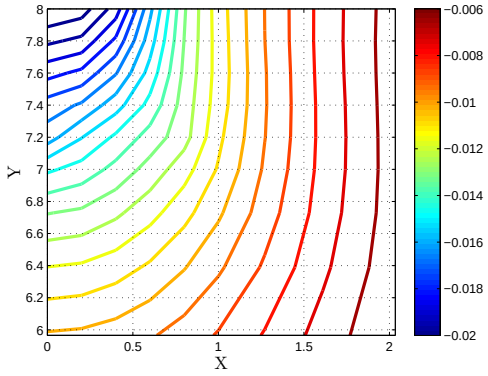


(c) max-ent without interface

Figure 18: Displacement ($u_y$) contours at $d_{max} = 3.8$ for the flexible strip footing problem

where $\mathbf{x}$ and $\mathbf{X}$ are the coordinates of a point in the current and reference configurations respectively. The work-conjugate stress and strain measures used in this paper are logarithmic strain $\boldsymbol{\varepsilon}$ and Kirchhoff stress $\boldsymbol{\tau}$ [42], which are given as [43]

$$\boldsymbol{\varepsilon} = \frac{1}{2} \ln \mathbf{b} \text{ and } \boldsymbol{\tau} = J\boldsymbol{\sigma}, \tag{29}$$

where $\mathbf{b}$ is the left Cauchy-Green strain tensor and $J$ is the determinant of the deformation gradient $\mathbf{F}$. In updated Lagrangian, the geometry is updated at each solution

step, which include the update of nodal coordinates, Gauss points and domain of influences. The shape functions and corresponding shape function derivatives are also calculated at each solution step. In updated Lagrangian formulations, the updated deformation gradient $\mathbf{F}_{n+1}$ at the end of increment $n+1$ is written as

$$\mathbf{F}_{n+1} = \Delta\mathbf{F}\,\mathbf{F}_n, \qquad \Delta\mathbf{F} = \left[\mathbf{I} - \delta\mathbf{F}\right]^{-1}, \qquad \delta\mathbf{F} = \sum_{i=1}^{L} \Delta\mathbf{u}_i \left[\begin{array}{c} \frac{\partial\phi}{\partial x} \\ \frac{\partial\phi}{\partial y} \end{array}\right]_i^T, \tag{30}$$

where $\Delta\mathbf{F}$ is an increment in the deformation gradient, $\mathbf{F}_n$ is the value of the deformation gradient at the end of previous increment, $\mathbf{I}$ is a $2 \times 2$ unit matrix in this case, $L$ is the number of nodes in support, $\Delta\mathbf{u_i}$ is the vector of incremental nodal parameters (or fictitious nodal values) and the shape function derivatives are calculated with reference to the updated geometry. The updated left Cauchy-Green strain matrix $\mathbf{b}_{n+1}$ is written as

$$\mathbf{b}_{n+1} = \Delta\mathbf{F}\,\mathbf{b}_n\,\Delta\mathbf{F}^T, \tag{31}$$

where $\mathbf{b}_n$ is the value of the left Cauchy-Green strain matrix at the end of previous increment and is obtained by rearranging Equation (29) in terms of $\mathbf{b}$. In the finite deformation case, the Newton-Raphson incremental-iterative procedure is used, i.e. load is applied incrementally in steps and convergence is sought for each increment, using

$$\mathbf{f}_{n+1}^{int}\left(\mathbf{u}_{n+1}\right) - \mathbf{f}_{n+1}^{ext} = \mathbf{oobf}_{n+1} = 0, \tag{32}$$

where $n+1$ is the global Newton-Raphson iteration counter, $\mathbf{f}_{n+1}^{int}$ and $\mathbf{f}_{n+1}^{ext}$ are the global internal and external force vectors respectively, $\mathbf{oobf}_{n+1}$ is the residual or out-of-balance force and $\mathbf{u}_{n+1}$ is a vector of nodal parameters or fictitious nodal values. The expression for the internal forces is given as

$$\mathbf{f}_{n+1}^{int} = \int_{\Omega} \mathbf{B}^T \boldsymbol{\sigma}\, d\Omega = \sum_{i=1}^{n_g} \mathbf{B}_i^T \boldsymbol{\sigma}_i \left|\mathbf{J}_i\right| w_i, \tag{33}$$

where $n_g$ are the total number of Gauss points within the problem domain, $\mathbf{B}_i$ is the strain displacement matrix at Gauss point $i$, consisting of the shape function derivatives calculated with reference to the updated nodal coordinates and the updated position of the Gauss points and $\mathbf{J}_i$ and $w_i$ are the Jacobian and weights associated with each Gauss points respectively. In this case, the equation for the global stiffness matrix is written as

$$K_{ij} = \int_{\Omega} \mathbf{G}_i^T \mathbf{a} \mathbf{G}_j d\Omega, \tag{34}$$

where $\mathbf{G}$ is a full stain-displacement matrix, calculated with reference to the updated nodal coordinates and Gauss points and is written as

$$\mathbf{G}_i = \left[\begin{array}{cc} \frac{\partial\phi_i}{\partial x} & 0 \\ 0 & \frac{\partial\phi_i}{\partial y} \\ \frac{\partial\phi_i}{\partial y} & 0 \\ 0 & \frac{\partial\phi_i}{\partial x} \end{array}\right] \tag{35}$$

and $\mathbf{a}$ is the spatial tangent and is written as

$$\mathbf{a} = \frac{1}{2J}\mathbf{DLB}^a - \mathbf{S} \tag{36}$$

where

$$\mathbf{L} = \frac{\partial \ln\left(\mathbf{b}\right)}{\partial \mathbf{b}}, \qquad \left(\mathbf{B}^a\right)_{ijkl} = \delta_{ik}\left(\mathbf{b}\right)_{jl} + \delta_{jk}\left(\mathbf{b}\right)_{il}, \qquad \left(\mathbf{S}\right)_{ijkl} = \left(\boldsymbol{\sigma}\right)_{il}\delta_{jk}. \tag{37}$$

Here **L** is the derivative of the logarithm of **b** with respect to its component, the detail of which is given in [44], while **S** is known as the non-symmetric stress corrector and $\delta_{ij}$ is the Kronecker delta.

For linear elastic or small strain problems, the FE or the EFG regions can be identified based on the problem dimensions, which is not applicable in case of large strain or finite deformation problems, as the geometry is changing during the solution. In these problems, it is necessary to attach a tag to each integration (Gauss) point to identify the FE or the EFG regions in the problem domain to which it belongs.

## 6. Numerical examples

Two numerical examples are now given in this section to demonstrate the implementation and performance of the current coupled FE-EFGM approach with geometrical nonlinearity.

**6.1. Infinite plate strip.** The first geometrically nonlinear problem solved by the coupled FE-EFGM formulation is an infinite plate strip subjected to uniformly distributed load $q$ and with simple supported edges, as shown in Figure 19. The dimen-

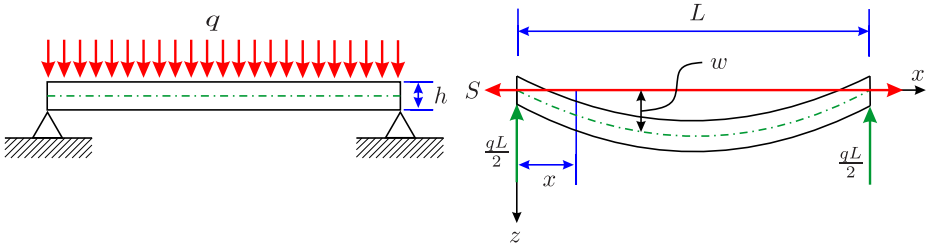


Figure 19: Infinite plate strip subjected to uniformly distributed load

sions of the plate are, length $L$ in $x$ direction, thickness $h$ in $z$ direction and with an infinite width in $y$ or out of plane direction. The analytical solution for this problem is given in [45], where it is given that the solution of the finite length plate approaches the one with infinite length when $\frac{L}{h} > 3$. The same problem is also solved in [46, 47] to validate the FEA finite deformation solution. The solution for the deflection $w$ at a distance $x$ is given as [45, 46]

$$w = \frac{qL^4}{16u^4D}\left[\frac{\cosh u\left(1-\frac{2x}{L}\right)}{\cosh u} - 1\right] + \frac{qL^2x}{8u^2D}\left(L-x\right) \tag{38}$$

where $D = \frac{Eh^3}{12(1-\upsilon^2)}$ is the flexural rigidity of the plate and $u^2 = \frac{SL^2}{4D}$, is found using

$$\frac{135}{16u^9}\left[\tanh u + \frac{u\tanh^2 u}{5} - u + \frac{2u^3}{15}\right] = \frac{E^2h^8}{\left(1-\upsilon^2\right)^2 q^2 L^8}. \tag{39}$$

where $S$ is the in-plane force. The maximum neutral axis deflection at $x = \frac{L}{2}$ is also given as

$$w_{max} = \frac{5qL^4}{384D}\left[\frac{\operatorname{sech} u - 1 + \frac{u^2}{2}}{\frac{5u^4}{24}}\right], \tag{40}$$

The problem was solved using $L = 10$, $h = 0.2$, $E = 1 \times 10^7$, $\nu = 0.25$ and $q = 40$, all in compatible units, while due to symmetry only half of the problem was modelled and the total pressure was applied in 20 equal step. In this case half of the remaining problem domain is discretized with the $40\,(20 \times 2)$ EFG background cells and the

remaining half with the $40\,(20 \times 2)$ FE, while the total number of nodes used is $123\,(41 \times 3)$. The coupled FE-EFGM undeformed configuration is shown in Figure 20(a) along with the deformed configuration for the same problem at the end of analysis. A comparison between numerical and analytical applied pressure versus the central displacement of the neutral axis normalized over the thickness of the plate is shown in Figure 20(b), giving excellent agreement. Furthermore, at the end of analysis a comparison between the numerical and analytical solution for the deflected profile normalized over the thickness of the plate is shown in Figure 20(c), again with excellent agreement. These results demonstrates that the proposed FE-EFGM approach can accurately capture the nonlinear behaviour of the plate.

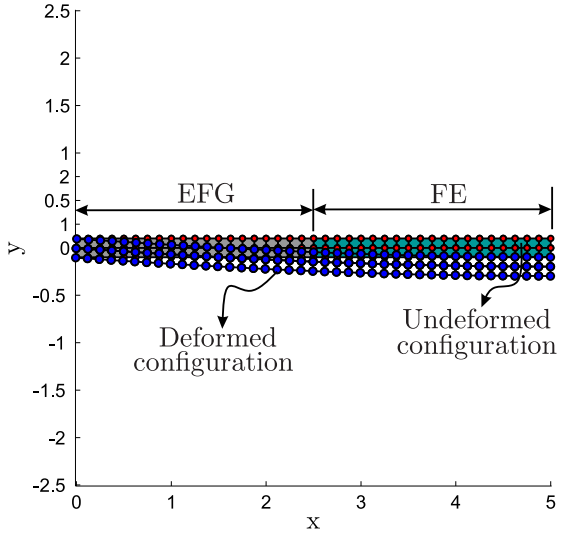


(a) Problem regions

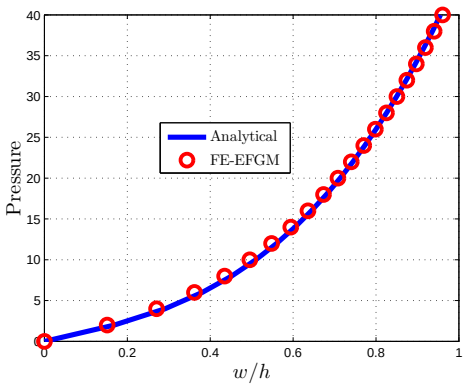


(b) Pressure vs $w/h$

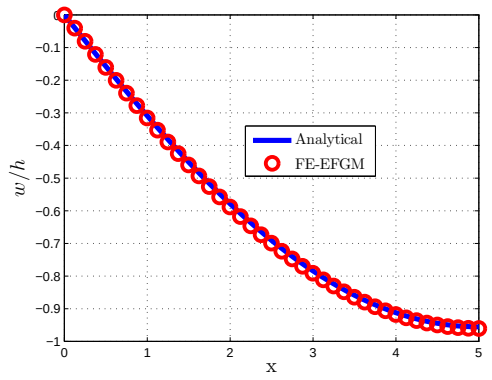


(c) $w/h$ vs $x$

Figure 20: Problem regions and results for the nonlinear infinite plate strip

**6.2. Elastic cantilever beam.** The second geometrically nonlinear problem is an elastic cantilever beam, subjected to uniformly distributed load (UDL) of $q$. The geometry, boundary condition and loading with deformed and undeformed configuration for the the cantilever beam with UDL is shown in Figure 21(a), where $L$, $H$, $B$ are the length, height and breadth in the $x$, $y$ and $z$ directions, $u_x$ and $u_y$ are the deformations in $x$ and $y$ direction respectively. The problem was solved with $L = 10$, $H = 1$, $B = 1$, $E = 1.2 \times 10^7$, $\nu = 0.2$ and $q = 10$. The pressure was applied to the neutral axis in 20 equal increments. Half of the beam was modelled with the $20\,(10 \times 2)$ EFG background cells, and the other half with $20\,(10 \times 2)$ FE. An un-

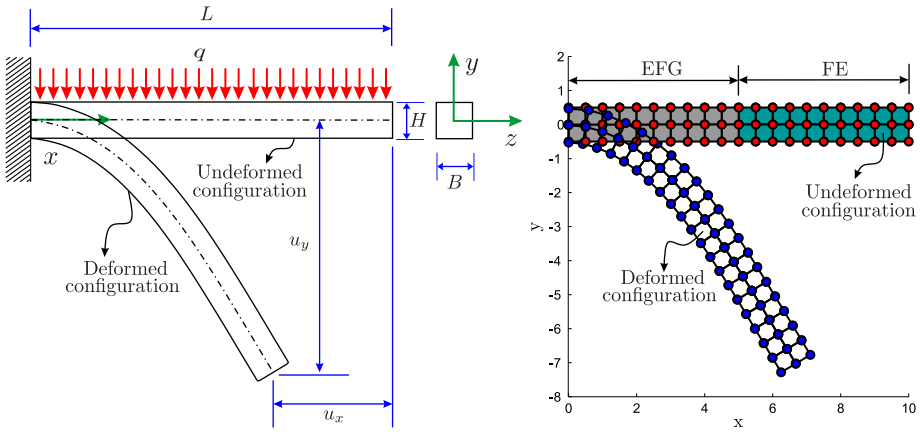


(a) Geometry

(b) Deformed and undeformed configuration

Figure 21: Geometry with undeformed and deformed configuration of the elastic cantilever beam problem with UDL

deformed hybrid FE-EFGM discretization is shown in Figure 21(b) with 42 $(21 \times 2)$ nodes. The final deformed configuration for this problem is also shown in Figure 21(b), which shows very large deformation. A comparison is also shown between the numerical and the reference solution [46] for the pressure versus $u_x$ and $u_y$ normalized over the length of the beam in Figure 22(a) and 22(b) respectively. Good agreement can be seen in these plots between the analytical and reference solution, which once again shows that the proposed coupled FE-EFGM approach can be used for nonlinear problems, even with very large deformation.

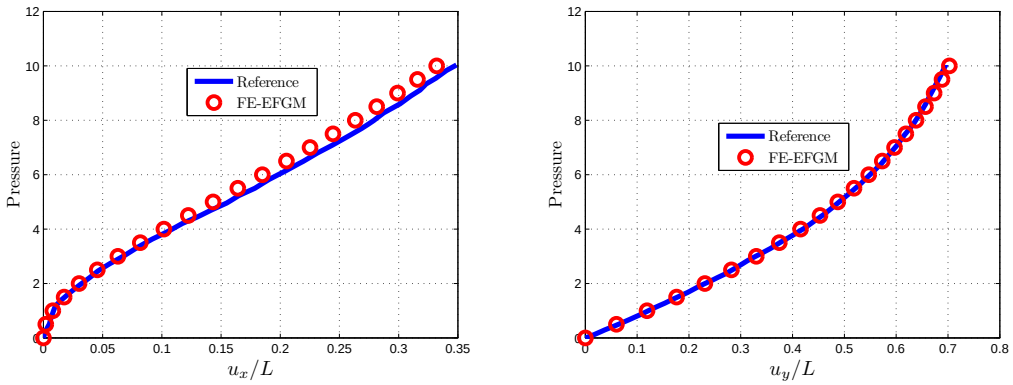


(a) Pressure vs $u_x/h$

(b) Pressure vs $u_y/h$

Figure 22: Problem regions and results for the nonlinear elastic cantilever beam

## 7. Concluding remarks

A new method of coupling the FEM with the EFGM based on the local max-ent shape functions has been proposed in this paper. These shape functions possess a weak Kronecker delta property at the boundaries, which provides a natural way to couple the regions without the use of a transition or an interface region. Results from the proposed coupled FE-EFGM have been compared with the corresponding results from the conventional FE-EFGM coupling, in which the MLS shape functions were used within the EFG region and interface elements were used between

the FE and the EFG regions. A comparison was also made with the case in which the MLS shape functions were used within the EFG region but with no interface region between the FE and the EFG. Very good agreement between the analytical and numerical solution was observed in all three cases with smaller domains of influence, as the MLS shape functions approach the FE shape functions with these smaller influence domains. However, the performance of the MLS in coupling the methods without an interface deteriorates as influence domains become larger, as the MLS shape functions will lose the approximate Kronecker delta property but even though the proposed coupling approach performs satisfactorily. Convergence plots of error in energy norm show that, the proposed coupling approach performs very close to conventional coupling, with almost the same rate of convergence, even with very large influence domains. The proposed coupling procedure was also extended to two-dimensional geometrically nonlinear problems. Once again, in these cases, it was shown from the solution of benchmark numerical examples that the proposed coupling approach performs satisfactorily, with excellent agreement between the numerical and corresponding analytical or reference results. Although lower-order elements were used in the FE region, it is straightforward to extend these ideas to high-order elements. Furthermore, only geometric nonlinearities are used in this paper but it is straightforward to include material nonlinearities.

## Acknowledgements

The first author is supported by an Overseas Research Students Awards Scheme award from Durham University.

## References

[1] T. Belytschko, Y. Y. Lu, and L. Gu. Element-free Galerkin methods. *International Journal for Numerical Methods in Engineering*, 37:229–256, 1994.

[2] T. Belytschko, D. Organ, and Y. Krongauz. A coupled finite element-element-free Galerkin method. *Computational Mechanics*, 17:186–195, 1995.

[3] D. J. Organ. *Numerical solution of dynamic fracture problems using the element-free Galerkin method*. PhD thesis, Northwestern Univeristy, 1996.

[4] C. C. Wu. *Meshless method for computer analysis of structure and media*. PhD thesis, University of Wisconsin-Madison, 2001.

[5] Y. Krongauz and T. Belytschko. Enforcement of essential boundary conditions in meshless approximations using finite elements. *Computer Methods in Applied Mechanics and Engineering*, 131:133 – 145, 1996.

[6] T. Belytschko, Y. Krongauz, J. Dolbow, and C. Gerlach. On the completeness of meshfree particle methods. *International Journal for Numerical Methods in Engineering*, 43(5):785–819, 1998.

[7] S. Fernández-Méndez and A. Huerta. Enrichment and coupling of the finite element and meshless methods. *International Journal for Numerical Methods in Engineering*, 48:1615–1636, 2000.

[8] A. Huerta, S. Fernández-Méndez, and W. K. Liu. A comparison of two formulations to blend finite elements and mesh-free methods. *Computer Methods in Applied Mechanics and Engineering*, 193:1105 – 1117, 2004.

[9] D. Hegen. Element-free Galerkin methods in combination with finite element approaches. *Computer Methods in Applied Mechanics and Engineering*, 135(1-2):143 – 166, 1996.

[10] T. Rabczuk and T. Belytschko. Application of particle methods to static fracture of reinforced concrete structures. *International Journal of Fracture*, 137:19–49, 2006.

[11] Y. T. Gu and L. C. Zhang. Coupling of the meshfree and finite element methods for determination of the crack tip fields. *Engineering Fracture Mechanics*, 75(5):986 – 1004, 2008.

[12] T. Rabczuk, S. P. Xiao, and M. Sauer. Coupling of mesh-free methods with finite elements: basic concepts and test results. *Communications in Numerical Methods in Engineering*, 22(10):1031–1065, 2006.

[13] H. P. Wang, C. T. Wu, Y. Guo, and M. E. Botkin. A coupled meshfree/finite element method for automotive crashworthiness simulations. *International Journal of Impact Engineering*, 36:1210 – 1222, 2009.

[14] B.N. Rao and S. Rahman. A coupled meshless-finite element method for fracture analysis of cracks. *International Journal of Pressure Vessels and Piping*, 78(9):647 – 657, 2001.

[15] Q.Z. Xiao and M. Dhanasekar. Coupling of FE and EFG using collocation approach. *Advances in Engineering Software*, 33:507 – 515, 2002.

[16] O. V. Estorff and J. Quan. Direct coupling of EFGM-FEM and EFGM-BEM for dynamic soilstructure interactions. *International Journal of Computational Methods*, 02(04):627–644, 2005.

[17] C. E. Shannon. A mathematical theory of communication. *The Bell Systems Technical Journal*, 27:379–423, 1948.

[18] A. I. Khinchin. *Mathematical foundation of information theory*. Dover Publications, Inc. , New York, 1957.

[19] E. T. Jaynes. Information theory and statistical mechanics. *Physical Review*, 106:620–630, 1957.

[20] E. T. Jaynes. Information theory and statistical mechanics-II. *Physical Review*, 108:171–190, 1957.

[21] N. Sukumar. Construction of polygonal interpolants: a maximum entropy approach. *International Journal for Numerical Methods in Engineering*, 61:2159–2181, 2004.

[22] M. Arroyo and M. Ortiz. Local *maximum-entropy* approximation schemes: a seamless bridge between finite elements and meshfree methods. *International Journal for Numerical Methods in Engineering*, 65:2167–2202, 2006.

[23] N. Sukumar and R. W. Wright. Overview and construction of meshfree basis functions: from moving least squares to entropy approximants. *International Journal for Numerical Methods in Engineering*, 70:181–205, 2007.

[24] C. J. Cyron, M. Arroyo, and M. Ortiz. Smooth, second order, non-negative meshfree approximants selected by maximum entropy. *International Journal for Numerical Methods in Engineering*, 79(13):1605–1632, 2009.

[25] D. González, E. Cueto, and M. Doblaré. A higher order method based on local maximum entropy approximation. *International Journal for Numerical Methods in Engineering*, 83(6):741–764, 2010.

[26] A. Rosolen, D. Mill e n, and M. Arroyo. On the optimum support size in meshfree methods: A variational adaptivity approach with maximum-entropy approximants. *International Journal for Numerical Methods in Engineering*, 82(7):868–895, 2010.

[27] A. Ortiz, M.A. Puso, and N. Sukumar. Maximum-entropy meshfree method for compressible and near-incompressible elasticity. *Computer Methods in Applied Mechanics and Engineering*, 199(25-28):1859 – 1871, 2010.

[28] A. Ortiz, M.A. Puso, and N. Sukumar. Maximum-entropy meshfree method for incompressible media problems. *Finite Elements in Analysis and Design*, 47(6):572 – 585, 2011.

[29] D. Millán, A. Rosolen, and M. Arroyo. Thin shell analysis from scattered points with maximum-entropy approximants. *International Journal for Numerical Methods in Engineering*, 85(6):723–751, 2011.

[30] G. Quaranta, S.K. Kunnath, and N. Sukumar. Maximum-entropy meshfree method for nonlinear static analysis of planar reinforced concrete structures. *Engineering Structures*, 42:179 – 189, 2012.

[31] A. Rosolen, D. Millán, and M. Arroyo. Second-order convex maximum entropy approximants with applications to high-order PDE. *International Journal for Numerical Methods in Engineering*, pages n/a–n/a, 2012.

[32] G. R. Liu. *Mesh Free Methods: Moving beyond the Finite Element Method*. CRC press, 2nd edition, 2010.

[33] I. M. Smith and D. V. Griffith. *Programming the Finite Element Method*. Wiley, Chichester, fourth edition, 2006.

[34] N. Sukumar. *Fortran 90 Library for* Maximum-Entropy Basis Functions. *User's Reference Manual Version 1.4. Code available at http://www.imechanica.org/node/3424*, 2008.

[35] J. Dolbow and T. Belytschko. An introduction to programming the meshless element-free Galerkin method. *Archives of Computational Methods in Engineering*, 5:207–241, 1998.

[36] O. C. Zienkiewicz and J. Z. Zhu. A simple error estimator and adaptive procedure for practical engineerng analysis. *International Journal for Numerical Methods in Engineering*, 24:337–357, 1987.

[37] S. P. Timoshenko and J. N. Goodier. *Theory of Elasticity*. McGraw-Hill, New York, 1970.

[38] C. E. Augarde and A. J. Deeks. The use of Timoshenko's exact solution for a cantilever beam in adaptive analysis. *Finite Elements in Analysis and Design*, 44:595 – 601, 2008.

[39] X. Zhuang, C. Heaney, and C.E. Augarde. On error control in the element-free galerkin method. *Engineering Analysis with Boundary Elements*, 36(3):351 – 360, 2012.

[40] A. J. Deeks and C. E. Augarde. A hybrid meshless local Petro-Galerkin method for unbounded domains. *Computer Methods in Applied Mechanics and Engineering*, 196(46):843 – 852, 2007.

[41] H. G. Poulos and E. H. Davis. *Elastic solutions for soil and rock mechanics*. John Wiley and Sons, New York, 1974.

[42] W. Ji, A. M. Waas, and Z. P. Bazant. Errors caused by non-work-conjugate stress and strain measures and necessary corrections in finite element programs. *Journal of Applied Mechanics*, 77(4):044504, 2010.

[43] W. M. Coombs, R. S. Crouch, and C. E. Augarde. 70-line 3D finite deformation elastoplastic finite-element code. In *Proc. Numerical Methods in Geotechnical Engineering (NUMGE), Trondheim, Norway*, pages 151–156, June 3-5 2010.

[44] C. Miehe. Comparison of two algorithms for the computation of fourth-order isotropic tensor functions. *Computers & Structures*, 66(1):37 – 43, 1998.

[45] S. P. Timoshenko and S. Woinkowsky-Krieger. *Theory of plates and shells*. McGraw-Hill Book Company, NY, 1959.

[46] T. K. Molstad. Finite deformation analysis using the finite element method. Master's thesis, The University of British Columbia, 1977.

[47] W. M. Coombs. *Finite deformation of particulate geomaterials: frictional and anisotropic Critical State elasto-plasticity*. PhD thesis, School of Engineering & Computing Sciences, Durham University, UK, 2011.